

Biomechanics in thrombus formation from direct cellular simulationsTing Ye¹,^{*} Xuejiao Zhang, Guansheng Li, and Sitong Wang¹*Department of Computational Mathematics, School of Mathematics, Jilin University, Changchun, 130012, China*

(Received 5 June 2020; revised 12 September 2020; accepted 2 October 2020; published 21 October 2020)

Numerically reproducing the process of thrombus formation is highly desired for understanding its mechanism but still remains challenging due to the polydisperse feature of blood components and their multiple biochemical or biomechanical behaviors involved. We numerically implemented a simplified version of the process from the perspective of biomechanics, using a mesoscale particle-based method, smoothed dissipative particle dynamics-immersed boundary method. This version covers the adhesion and aggregation of platelets (PLTs), the deformation and aggregation of red blood cells (RBCs), and the interaction between PLTs and RBCs, as well as the blockage of microvessels. Four critical factors that can affect thrombus formation were investigated: the velocity of blood flow, the adhesive ability of PLTs, the interaction strength between PLTs and RBCs, and the deformability of RBCs. Increasing the velocity of blood flow was found to be the most effective way to reduce the microvessel blockage, and reducing the adhesive ability of PLTs is also a direct and efficient way. However, decreasing the interaction strength between PLTs and RBCs sometimes does not alleviate thrombus formation, and similarly, increasing the deformability of RBCs does not have a significant improvement for the severely blocked microvessel. These results imply that maintaining high-rate blood flow plays a crucial role in the prevention and treatment of thrombosis, which is even more effective than antiplatelet or anticoagulant drugs. The drugs or treatments concentrating on reducing the PLT-RBC interaction or softening the RBCs may not have a significant effect on the thrombosis.

DOI: [10.1103/PhysRevE.102.042410](https://doi.org/10.1103/PhysRevE.102.042410)**I. INTRODUCTION**

Thrombotic diseases, such as strokes and ischemic heart diseases, remain the leading causes of death and disability worldwide [1]. Thrombus formation is a complex, dynamic, and multistep process, involving biochemical reactions, mechanical stimulation, hemodynamics, and other factors. In recent years, there has been increasing interest in the mechanical factors in thrombus formation, from the macrofluidic environment to the cellular biomechanics and the molecular dynamics [2]. However, the whole picture is still incomplete and continually evolving, and especially at the cellular and molecular scales, it is still challenging to recapitulate mechanical micro-environments, from either experimental [3] or modeling perspectives [4,5].

At the macroscale level, numerous studies have focused on the mechanics of blood clots, blood rheology, and the interaction between whole clots and the fluidic environment, with the aid of rheometers, thromboelastography, platelet-contraction cytometers, etc. [6,7]. Blood clots are characterized into many types, such as platelet-rich and erythrocyte-rich, and different types can be greatly different in mechanical properties [8]. Generally, they exhibit viscoelastic behaviors, having both elasticity like rubbers and viscosity like fluids. These viscoelastic clots can reduce the velocity of blood flow and increase the blood viscosity, changing blood rheology [9]. In turn, the changes of blood rheology can result in the abnormality of shear stress in the fluidic environment, influencing

the formation of the blood clots. Therefore, blood rheology is often regarded clinically as one of the important biomarkers of thrombosis [10].

Although the macroscale techniques have improved our understanding of the changes in some important factors during thrombus formation, the underlying mechanisms of these macrofactors are often rooted in individual cells and even molecules [11]. Therefore, a variety of studies have been done with single-cell or single-molecule analysis to further explain these factors, using microfluidic devices, atomic force microscopy, optical tweezers, etc. These studies typically cover the biomechanics of single cells, aggregation of multiple cells, adhesion of cells at the injury site, and mechanical regulation of signaling cascades, as well as the mechanical behaviors of individual molecules [12–18]. At this scale, thrombus formation has been found to strongly depend on the adhesion and aggregation of platelets (PLTs) [19–21]. PLTs can be biochemically activated by binding to the exposed adhesive proteins such as collagen and von Willebrand factor (vWF) and adhere onto the subendothelial matrix at the injury site, leading to PLT adhesion. They can also be activated by binding to soluble agonists such as ADP and thrombin, which triggers cytoskeletal reorganization, shape spreading, and granule release, making the PLT adhesion firmer and simultaneously leading to the PLT aggregation. In parallel, it has been found that these processes are also regulated biomechanically, where the shear force pulling the receptors on PLTs triggers mechanosignals and leads to intracellular signal mechanotransduction, that is, the external biomechanical stimulations are transduced into biological signals [22,23]. More recently, Chen *et al.* [24] even discovered that the PLTs can be activated only by biomechanical stimulation,

^{*}yeting@jlu.edu.cn.

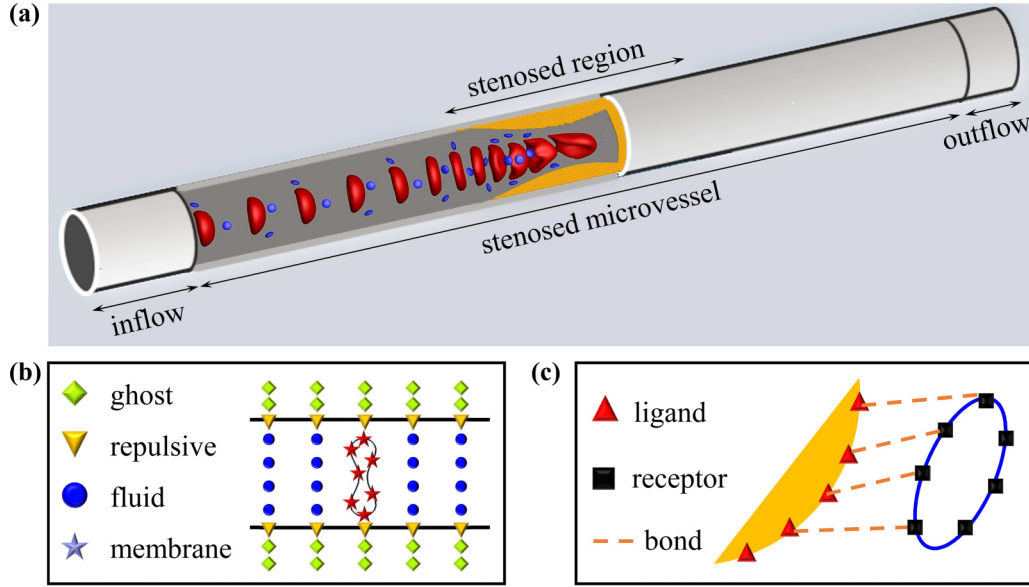


FIG. 1. Description of simulation problem. A straight microvessel (a) is considered, and it has a ring stenosis region where the PLTs may experience adhesion and aggregation. An inflow and an outflow region are added at the left and right sides of the microvessel, for handling the inflow and outflow boundary conditions, respectively. In simulations, the whole domain is discretized into a set of particles, as well as the PLTs and RBCs (b). To characterize the PLT adhesion, the ligands and receptors are modeled as discrete particles on the surface of the stenosed region and the PLT, respectively (c).

without any biochemical stimulations. Additionally, many studies have also been done to reveal the roles of the red blood cells (RBCs) during thrombus formation, such as their movement, aggregation, and deformation [25]. As we know, the RBCs not only contribute to blood rheology, but also affect the trajectories of PLTs due to their intercellular interaction. More importantly, some blood clots are mainly made up of RBCs, such that their mechanical properties will certainly affect thrombus formation.

A large number of simulation studies have also been performed in an attempt to numerically reproduce the process of thrombus formation, from the perspectives of hydrodynamics, coagulation cascade, PLT activation, cell mechanics, receptor-ligand adhesion, fibrin network, and so on [26]. For instance, pure-fluid simulations treat blood as pure fluid without considering blood components to study the evolution of the fluid field around a thrombus [27,28]. Single-PLT simulations consider a single rigid or deformable PLT in fluidic environment and mainly study its adhesion by forming or dissociating receptor-ligand bonds [29–31]. Massive-PLT simulations often focus on a large number of rigid PLTs and mainly study their aggregation, adhesion, and margination [32,33]. However, few previous studies have included all the perspectives in realistic three-dimensional (3D) models and reproduced the whole process of thrombus formation, due to the challenge of combining them in simulation tools [5]. In macroscopic models, it is difficult to couple the biochemical processes, such as the formation and dissociation of bonds, while in microscopic models, it is unaffordable in terms of computer resources for considering the fluidic environment and the behaviors of a large number of cells.

More recently, we have developed a mesoscopic model, the smoothed dissipative particle dynamics-immersed boundary

method (SDPD-IBM) [34,35], to investigate the behaviors of blood components in very complex microvessels. This model allows us not only to perform a large-scale simulation of the blood flow, compared with the microscale numerical methods, but also to capture some molecular details more easily, e.g., the adhesion and aggregation binding of cells, compared with the macroscale numerical methods. Using this model, we have studied the deformation and aggregation of many RBCs in simple or complex microvessels [34,36] and have numerically designed the microfluidic chips to measure the cell mechanics and separate blood plasma [37,38], among other things. In the present work, we still use SDPD-IBM and make an attempt to numerically reproduce the process of thrombus formation at the cellular scale, including the adhesion, aggregation, and deformation of a large number of PLTs, the aggregation and deformation of a large number of RBCs, and the interaction between the PLTs and RBCs. We pay more attention to the conditions under which the microvessel is blocked more easily and the roles of the biomechanical forces in such conditions.

II. METHODS

A. Problem description

A straight microvessel with a ring stenosis is considered [see Fig. 1(a)], 15 μm and 150 μm in diameter and length, respectively, and the narrowest diameter at the stenosis is 7.5 μm . The stenosis is 50 μm in length, one third of the whole microvessel, where the PLTs may adhere and aggregate. An inflow region with 20 μm long is added at the left side of the microvessel for handling the inflow boundary condition. Similarly, an outflow region with 10 μm is added at its right side for the outflow boundary condition.

Because the numerical model, SDPD-IBM, is a particle-based method, the whole computational domain is discretized into a set of particles [see Fig. 1(b)]. There are four types of particles, including 23 027 fluid particles, 19 357 ghost particles, 36 908 repulsive particles, and 613 (or 60) membrane particles for the membrane of each RBC (or PLT). The fluid particles represent the fluid in the microvessel; both the ghost and repulsive particles are used to model the microvessel wall, and the membrane particles represent the RBC's or PLT's membrane. Moreover, in order to model the PLT adhesion, there are 8492 ligands on the surface of stenosed region, and 60 receptors on the surface of each PLT [see Fig. 1(c)]. It should be noted that the numbers of receptors and ligands are much smaller than the real physical values due to the limit of computational resources. Here a receptor (or ligand) represents a large number of real receptors (or ligands) from the viewpoint of a coarse-graining idea, and the similar behaviors with the real adhesion are provided by adjusting the model parameters. In order to show the reliability of this procedure, we have studied the motion and adhesion of a PLT in our previous work (see the Supplemental Material [39] for validation of the behaviors of a PLT). In total there are about 100 000 particles for a typical simulation case with 25 RBCs and 75 PLTs, and its computational cost is about 96×48 core · hour, i.e., running the codes for two days with 96 cores.

B. Mathematical models

In SDPD-IBM, each fluid particles follows Newton's second law of motion [34,35],

$$d\mathbf{x}_i = \mathbf{v}_i dt, \quad (1)$$

$$m d\mathbf{v}_i = \mathbf{F}_C dt + \mathbf{F}_D dt + \mathbf{F}_R + \mathbf{F}_G dt + \mathbf{F}_B dt, \quad (2)$$

and each membrane particle is evolved by

$$\frac{d\mathbf{X}_k}{dt} = \sum_i \beta_{ik} \mathbf{v}_i, \quad (3)$$

where t is the time, m is the mass of a fluid particle, \mathbf{x}_i and \mathbf{v}_i are the coordinate and velocity of the fluid particle i , respectively, \mathbf{X}_k is the position of the membrane particle k , and β_{ik} is the weighted coefficient determined by the kernel function of SDPD. The forces \mathbf{F}_C , \mathbf{F}_D , and \mathbf{F}_R are the conservative, dissipative, and random forces, respectively, and they are related to the compressibility, viscosity, and thermal fluctuation of fluid. The force \mathbf{F}_G is the externally applied force to drive the fluid flow. The force \mathbf{F}_B is the singular force from the cell membrane, here consisting of three types of membrane forces: the deformation force \mathbf{F}_k^{def} , aggregation force \mathbf{F}_k^{agg} , and adhesion force \mathbf{F}_k^{adh} for describing the cell deformation, aggregation, and adhesion, respectively:

$$\mathbf{F}_B = \sum_k \beta_{ik} (\mathbf{F}_k^{def} + \mathbf{F}_k^{agg} + \mathbf{F}_k^{adh}). \quad (4)$$

See the Appendix for more details about the mathematical models and their validations that have been performed in our previous work (see Ref. [39] for the validations of the mathematical models).

C. Numerical methods

The velocity-Verlet algorithm is used to solve governing equations (1)–(4) for obtaining the positions and velocities of the fluid particles, as well as the positions of the PLTs and RBCs [42,43] (see the Appendix). Three types of boundary conditions are considered: the solid boundary condition on the microvessel wall, the inflow boundary condition at the inlet, and the outflow boundary condition at the outlet. The solid boundary condition is implemented by using the ghost and repulsive particles [44] [see Fig. 1(b)]. The ghost particles are placed outside the solid wall to improve the numerical accuracy near the wall, while the repulsive particles are exactly placed on the solid wall to prevent the fluid particles from penetrating the solid wall. The inflow boundary condition is implemented by adding an inflow region at the left of the microvessel [see Fig. 1(a)], which is treated as a generation region that can continuously generate new fluid particles and new cells flowing into the microvessel [35]. Hence, a fully developed flow is ensured to be duplicated into the microvessel from the inflow region. The outflow boundary condition is similarly implemented by adding an outflow region at the right of the microvessel. It is treated as a deletion region, in which the fluid particles and cells are deleted, but their mass and momentum are compensated within an error of 10^{-4} [35]. Hence, the total mass and momentum of the system are almost conserved and not lost due to the deletion of fluid particles and cells.

D. Simulation cases

A nondimensionalization procedure is performed, and several important dimensionless groups are identified (see the Appendix). Among them, three dimensionless groups are examined to identify the effects of (1) the adhesion of PLTs Ca_A , (2) the interaction between PLTs and RBCs Ca_I , and (3) the deformation of RBCs Ca_S , on thrombus formation, where Ca in each case is the capillary number. Five simulation cases are designed as follows, and their physical and simulation parameters are listed in Table I.

Case A: Two RBCs are equidistantly placed into the inflow region at the initial state, corresponding to the initial RBC hematocrit of 5.3%, and four PLTs are also equidistantly placed into that region. A force of $\mathbf{F}_G = 0.2$ pN is externally applied for each fluid particle to drive the fluid flow, which generates a mean velocity of $v_m = 1.5$ cm/s for the flow without cells. All other physical parameters can be found in Table I. Hence, the capillary numbers are calculated to be $Ca_A = 0.12$, $Ca_I = 1.45$, and $Ca_S = 0.24$. This case serves as a comparison basis with other cases that differ from the current case in only one aspect.

Case B: A weak adhesion of PLTs is considered by decreasing the adhesion strength twice, i.e., $\tilde{E}_A = 6.0 \times 10^{-6}$ N/m, to examine the adhesion force of PLTs. All other parameters remain the same as in Case A. Hence, in this case $Ca_A = 0.24$, $Ca_I = 1.45$, and $Ca_S = 0.24$.

Case C: A strong aggregation between the PLTs and RBCs is considered by increasing their aggregation strength tenfold, i.e., $\tilde{E}_I = 1.0 \times 10^{-5}$ N/m, to examine the aggregation force between the PLTs and RBCs. All other parameters remain the

TABLE I. Physical and simulation parameters.

Parameters		Physical values	Scaling quantities	Simulation values
Fluid	Density (ρ)	10^3 kg/m^3	m'/l'^3	8
	Viscosity (η)	10^{-4} Pa s	$\sqrt{m'\epsilon'}/l'^2$	197
	External force (F_G)	$2 \times 10^{-13} \text{ N}$	ϵ'/l'	100
RBC	Shear modulus (E_S)	$6.0 \times 10^{-6} \text{ N/m}$ [40]	ϵ'/l'^2	5.794×10^3
	Bending modulus (E_B)	$2.0 \times 10^{-19} \text{ J}$ [40]	ϵ'	50
	Dilation modulus (E_D)	$1.264 \times 10^{-4} \text{ N/m}$	ϵ'/l'^2	1.216×10^5
	Aggregation strength (E_I)	$1.0 \times 10^{-6} \text{ N/m}$ [41]	ϵ'/l'^2	965
	Scaling factor (β)	$3.84 \mu\text{m}^{-1}$ [41]	$1/l'$	7.68
	Zero-force separation (r_0)	$0.49 \mu\text{m}$ [41]	l'	0.245
	Shear modulus (\tilde{E}_S)	$5.0 \times 10^{-4} \text{ N/m}$ [31]	ϵ'/l'^2	4.828×10^5
PLT	Bending modulus (\tilde{E}_B)	$8.29 \times 10^{-19} \text{ J}$ [31]	ϵ'	200
	Dilation modulus (\tilde{E}_D)	$1.621 \times 10^{-3} \text{ J}$	ϵ'/l'^2	1.565×10^6
	Aggregation strength (\tilde{E}_I)	$1.0 \times 10^{-6} \text{ N/m}$ [41]	ϵ'/l'^2	965
	Scaling factor ($\tilde{\beta}$)	$3.84 \mu\text{m}^{-1}$ [41]	$1/l'$	7.68
	Zero-force separation (\tilde{r}_0)	$0.49 \mu\text{m}$ [41]	l'	0.245
	Adhesion strength (\tilde{E}_A)	$1.2 \times 10^{-5} \text{ N/m}$	ϵ'/l'^2	1.159×10^4
	Equilibrium length ($\tilde{\lambda}$)	$0.5 \mu\text{m}$	l'	0.25
	Equilibrium forming rate (\tilde{k}_f^0)	$4 \times 10^3 \text{ s}^{-1}$	$\sqrt{\epsilon'/m'}/l'$	3.9
	Equilibrium rupturing rate (\tilde{k}_r^0)	4 s^{-1}	$\sqrt{\epsilon'/m'}/l'$	3.9×10^{-3}
	Forming strength ($\tilde{\sigma}_f$)	$1.2 \times 10^{-7} \text{ N/m}$	ϵ'/l'^2	116
	Rupturing strength ($\tilde{\sigma}_r$)	$2.4 \times 10^{-9} \text{ N/m}$	ϵ'/l'^2	2.32
	Aggregation strength (\hat{E}_I)	$1.0 \times 10^{-6} \text{ N/m}$ [41]	ϵ'/l'^2	965
	Scaling factor ($\hat{\beta}$)	$3.84 \mu\text{m}^{-1}$ [41]	$1/l'$	7.68
	Zero-force separation (\hat{r}_0)	$0.49 \mu\text{m}$ [41]	l'	0.245

^aThe aggregation parameters between PLTs and RBCs.

same as in Case A. Hence, in this case $\text{Ca}_A = 0.12$, $\text{Ca}_I = 0.145$, and $\text{Ca}_S = 0.24$.

Case D: The softer RBCs are considered by decreasing the shear modulus of the RBCs tenfold, i.e., $E_S = 6.0 \times 10^{-7} \text{ N/m}$, to examine the deformation force of the RBCs. All other parameters remain the same as in Case A. Hence, in this case $\text{Ca}_A = 0.12$, $\text{Ca}_I = 1.45$, and $\text{Ca}_S = 2.4$.

Case E: A large flow velocity is considered by doubling the externally applied force, i.e., $F_G = 0.4 \text{ pN}$, which generates a mean velocity of $v_m = 3.0 \text{ cm/s}$ for the flow without cells. All other parameters remain the same as in Case A. Hence, the three capillary numbers are calculated to be $\text{Ca}_A = 0.24$, $\text{Ca}_I = 2.9$, and $\text{Ca}_S = 0.48$, which is equivalent to reducing the adhesion strength of PLTs, aggregation strength between RBCs and PLTs, and shear modulus of RBCs twice simultaneously.

It is found that the capillary number is changed 10 times in Case C for Ca_I and Case D for Ca_S compared with Case A, but only twice in Case B for Ca_A . This is because the PLTs are found to be not firmly adhered onto the stenosed region in Case B, when the adhesion strength is decreased twice. If decreasing it 10 times, the PLTs are definitely not firmly adhered onto the stenosed region. Similarly, it is found in Case E that the microvessel is not blocked at all when increasing the velocity of blood flow twice, not to mention 10 times.

III. RESULTS

A. Overview of thrombus formation

The process of thrombus formation in a stenosed microvessel (Case A) is shown in Fig. 2. As the time elapses, both

the PLTs and RBCs gradually flow into the microvessel. The RBCs deform into a parachute shape, and first achieve the stenosed part with a relatively high velocity, because they move along the microvessel centerline. The PLTs have almost no deformation and are second to the RBCs reaching the stenosed part along the microvessel wall. Since the stenosed surface is covered with many adhesive ligands, these PLTs are adhered onto the surface via forming the ligand-receptor bonds. When more and more PLTs are adhered and aggregated in the stenosed region, they start to capture the RBCs approaching them. As a result, the RBCs gather at the stenosed region, causing the microvessel blockage. There are three key phenomena occurring in this process of thrombus formation: the PLTs adhered onto the stenosed surface, the PLTs capturing the RBCs, and the RBC deformation. It is conceivable that the thrombus may not be formed if the PLTs are not adhered. Similarly, if the RBCs are not captured by the aggregated PLTs, the thrombus may also not appear. In addition, if the RBCs become rigid, the microvessel may be blocked more easily when passing through the stenosed region. In the present work, therefore, we mainly pay our attention to answering these questions.

Figure 3 shows the mechanical behaviors of a PLT and a RBC, including the adhesion of a PLT [Figs. 3(a)–3(c)], the interaction between a PLT and a RBC [Figs. 3(d)–3(f)], and the deformation of a RBC [Figs. 3(g)–3(i)]. The PLT undergoes a tumbling motion before arriving at the stenosed region, where it tumbles forward and has almost no deformation. After reaching the stenosed region, it is gradually adhered onto the stenosed surface and finally exhibits a firm adhesion mode. The previous studies [45,46] have shown that a cell

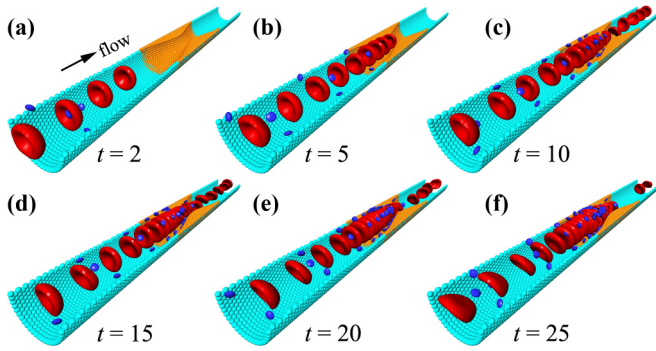


FIG. 2. Overview of thrombus formation in a stenosed microvessel (Case A; see Ref. [39] for the video of Case A). At the initial state, six cells (two RBCs and four PLTs) that are placed in the inflow region (the leftmost of the microvessel) are ready to flow into the microvessel. At $t = 2$ (a), eight cells (four RBCs and four PLTs) have already flowed into the microvessel, but not yet arrived at the stenosed region. At $t = 5$ (b), there are 21 cells (nine RBCs and 12 PLTs) moving into the microvessel, and the leading RBCs are squeezed for passing through the stenosis while the leading PLTs are just arriving at the stenosed region. At $t = 10$ (c), there is a RBC flowing out of the microvessel, and 43 cells (18 RBCs and 25 PLTs) are still in the microvessel. The PLTs start to be adhered onto the stenosed surface, such that they cannot move forward with the fluid flow anymore, but the RBCs can still pass through the stenosis successfully. At $t = 15$ (d), seven RBCs move out of the microvessel, but 62 cells (21 RBCs and 41 PLTs) are in the microvessel. More PLTs are adhered onto the stenosed surface, and some RBCs happen to aggregate in the stenosed region. At $t = 20$ (e), there are 15 RBCs flowing out of the microvessel, and 80 cells (21 RBCs 59 PLTs) are still in the microvessel. At $t = 25$ (f), 21 RBCs move out of the microvessel, and 101 cells (24 RBCs and 77 PLTs) are still in the microvessel. Most of the cells in the microvessel are piled up at the stenosed region, so that the microvessel is almost blocked completely.

in a simple shear flow may undergo three typical motions: tumbling, trembling, and tank-treading modes. Which modes is exhibited depends on several parameters, such as flow velocity, cell rigidity, etc. In general, a rigid cell is more likely to undergo a tumbling motion. Because the PLT is barely deformed with a large rigidity, it often exhibits a tumbling mode. More especially, the tumbling motion for a PLT is also called a “pole-vaulting” motion, first moving toward and contacting the microvessel wall, and then bounced away from the wall [29]. In addition, it has been shown [47] that a cell often exhibits three typical adhesion modes: firm, rolling, and detachment adhesion. Which mode is present depends on the competition between forming new bonds and dissociating the existing bonds. In the present case, the new bonds start to be formed from $t = 7.5$, and then a slight oscillation is present until $t = 15$ due to the existence of both forming bonds and dissociating bonds. After that, the PLT is firmly adhered onto the stenosed surface, and no existing bonds are dissociated, such that the bond number almost maintains a constant value of about 55. Therefore, a firm adhesion occurs, with a nearly constant adhesion force of 7×10^4 , i.e., 145 pN, while a rupture force for the P-selectin or PSGL-1 bond was reported to vary from 115 to 165 pN with different pulling velocities [48].

This adhesion force pulls the PLT to a fixed position of $X_c = 35$ and leads to the PLT’s velocity approach zero finally.

The interaction between a PLT and a RBC is examined to understand the capture of RBCs by the PLTs. It is difficult to analyze this interaction in the stenosed region, because there are many PLTs entangled with this RBC. As such, we focus on a pair of RBC and PLT which do not yet arrive at the stenosed region. Before $t = 3.5$, the PLT is located in the front of the RBC and they are far away, such that there is no interaction between them. From $t = 3.5$, the RBC enters into the interaction domain of the PLT, i.e., there is an aggregation force between them. At around $t = 4$, the RBC catches up to the PLT, subsequently achieving the maximum interaction because they are closest at this moment. Until $t = 5.5$, the RBC starts to leave away from the PLT interaction domain, and their interaction disappears again. Their interaction is also read from the resultant aggregation forces acting on the RBC and PLT, respectively. These forces are equal in magnitude but opposite in direction for each component. Moreover, at about $t = 4$, the x components of the aggregation force are switched between the PLT and RBC in direction, because their relative positions are switched. Hence, this cell pair exhibit an attractive interaction during the whole stage. The maximum aggregation force is about 1.2×10^3 , i.e., 2.5 pN in magnitude, while an interaction force between two RBCs was reported to be 8.4 ± 1.1 pN [49]. In order to catch a RBC by PLTs, many PLTs are required to exert such attractive force. Whether a RBC is caught in the stenosed region will mainly depend on the competition between this attractive force from the PLTs and the shear force from the fluid flow. The latter force is roughly evaluated as the externally applied force acting on a RBC, and thus it is about 122.6 pN. Neglecting the aggregation forces from other RBCs, therefore, there are at least 50 PLTs required to interact with this RBC for catching it. Note that here the effect of the stenosis on the RBC is also not taken into account.

The deformation of a RBC is examined to understand how it deforms itself to pass through the stenosis. The RBC exhibits a typical parachute deformation before arriving at the stenosed region, while in the stenosed region, it is squeezed severely by the thrombus and exhibits an irregular deformation due to its interaction with many PLTs. The cell deformation is related to the deformation force, and the more obvious the deformation is, the larger the deformation force. Note that this deformation force is an internal force, so that its resultant is zero for each cell. However, for a membrane particle, the maximum deformation force is evaluated to be about 4.5×10^3 , i.e., 9 pN. To quantitatively measure the cell deformation, a deformation index τ , also called asphericity, is introduced [50],

$$\tau = \frac{1}{2} \frac{(I_1 - I_2)^2 + (I_2 - I_3)^2 + (I_3 - I_1)^2}{(I_1 + I_2 + I_3)^2}, \quad (5)$$

where I_1 , I_2 and I_3 are the principal moments of inertia of the cell, i.e., the eigenvalues of the moment-of-inertia tensor. A general rule is that the rounder a cell, the smaller its asphericity, and it is zero if the cell is deformed into a spherical shape. At $t = 12.5$, the RBC moves into the microvessel, and until $t = 14$ it has a slight deformation with a flat asphericity. From $t = 14$ to 16, the RBC arrives in the front of the stenosis,

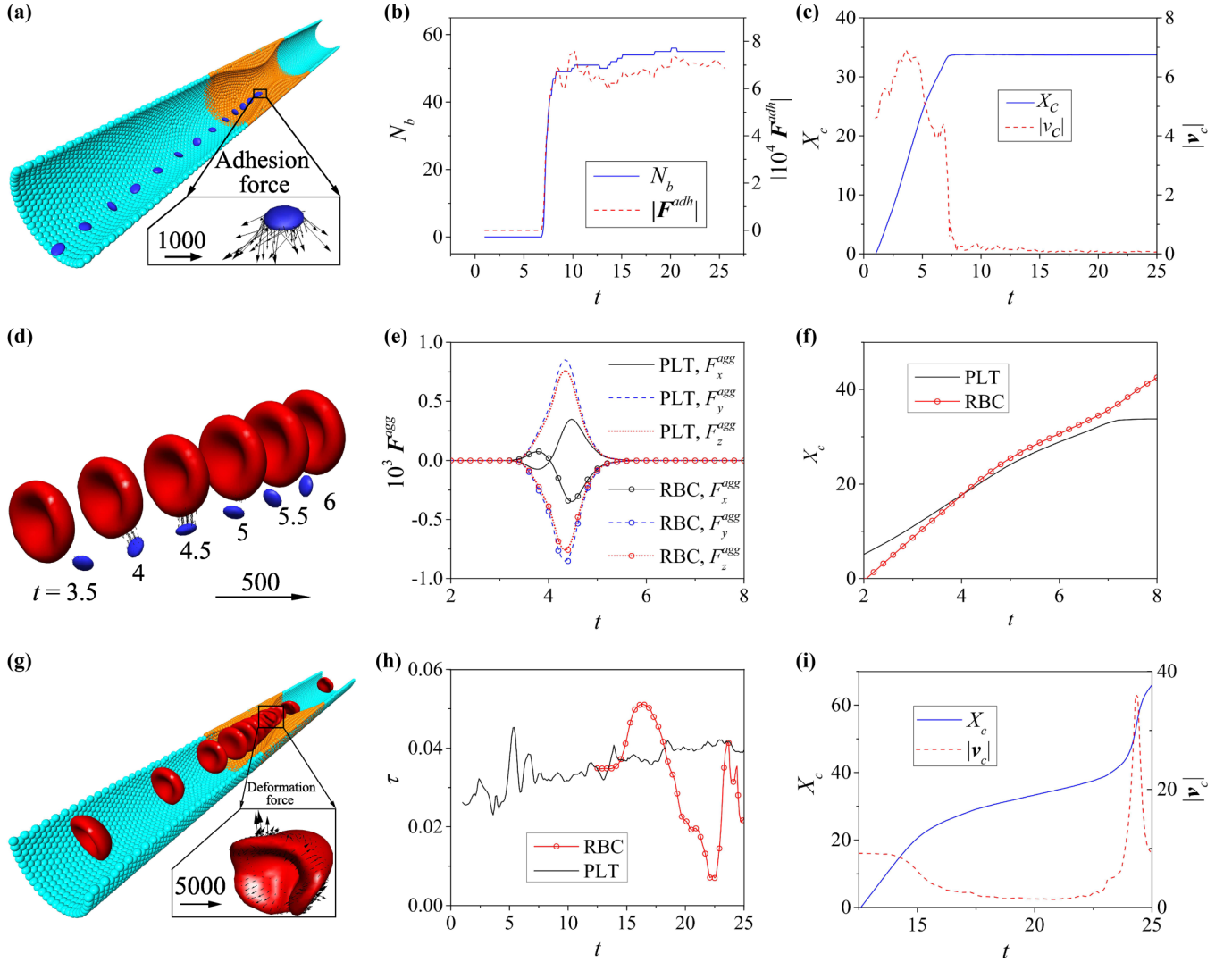


FIG. 3. Mechanical behaviors of a PLT and a RBC in the stenosed microvessel. One of the PLTs is selected to analyze the adhesion behaviors of a PLT in thrombus formation (a–c). There are 49 PLT snapshots taken from $t = 1$ to 25 with a time interval of 0.5, while the latter 37 snapshots are almost overlapped at the same position, because the PLT is subject to a strong adhesion force (a). The adhesion of the PLT is quantitatively described by the evolution of the number N_b of formed receptor-ligand bonds and the magnitude ($|F^{adh}|$) of the adhesion force acting on the PLT, respectively (b). The movement of the PLT is quantitatively described by the evolution of the x component X_c of the PLT centroid and the velocity magnitude $|v_c|$ of the PLT, respectively (c). A pair of RBC and PLT are considered to analyze the interaction between them (d–f). Their aggregation forces start to appear at about $t = 3.5$, then strengthens at about $t = 4.5$, and finally disappears about at $t = 6$ (d), and the corresponding resultant forces F^{agg} are equal in magnitude but opposite in direction (e). At about $t = 4$, the RBC catches up to the PLT along the flow direction, which can be read from the x component X_c of their centroids (f). At this moment, the direction of the x -component aggregation force between the RBC and PLT is switched, so that the RBC and PLT attract each other during this interaction stage. One of the RBCs is also selected to analyze the deformation behaviors of a RBC in thrombus formation (g–i). There are 13 snapshots taken from $t = 13$ to 25 with a time interval of 1.0, and from $t = 16$ to 24 the RBC stays in the stenosed region (g). The deformation of the RBC is quantitatively described by the evolution of the deformation index τ , and for comparison the deformation index of a PLT is added (h). The movement of the RBC is quantitatively described by the x component X_c of the RBC centroid and its velocity magnitude $|v_c|$, respectively (i).

and its velocity decreases due to the blockage in the stenosed region, as shown in Fig. 3(i). The RBC is squeezed in the axial direction, but elongated in the radial direction, such that the asphericity increases because it looks less round. From $t = 16$ to 22.5, the RBC moves into the upstream of the stenosis, and it is quickly squeezed by the stenosis. Hence, its velocity becomes low, and its asphericity decreases quickly. After $t = 22.5$, the RBC moves to the downstream of the stenosis and subsequently leaves the stenosis. Because the microvessel

space increases suddenly, the RBC gets a sudden increase in speed and quickly recovers its original shape, leading to a sharp increase of the asphericity. Near about $t = 25$, the RBC approaches the microvessel outlet. Because the flow velocity at the outlet is as low as that at the inlet, the RBC decreases its velocity and is squeezed again in the axial direction. Hence, its asphericity decreases again near $t = 25$. The RBC deformability allows it to pass through the stenosis successfully, having a positive effect on preventing the thrombosis. It is definite

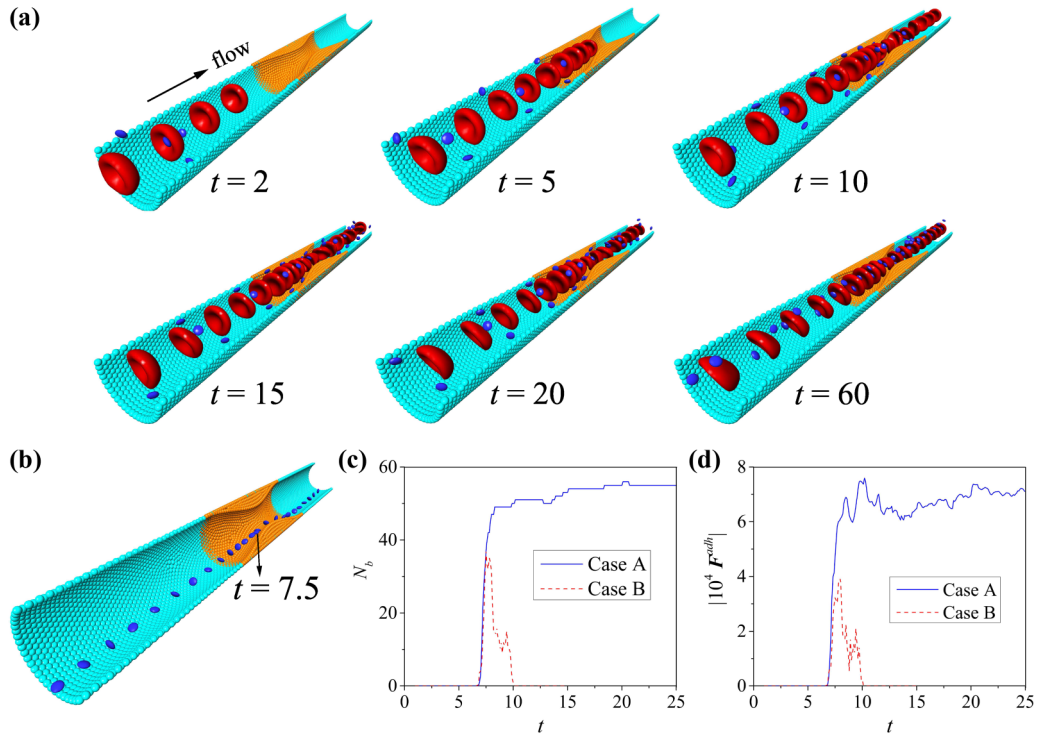


FIG. 4. Effect of the adhesive ability of PLTs (Case B; see Ref. [39] for the video of Case B). (a) Six snapshots of the PLTs and RBCs under a weak adhesion. At $t = 2$ and 5 , the PLTs and RBCs have the same behaviors as those in Case A. At $t = 10$, there is also a RBC flowing out of the microvessel, and 43 cells (18 RBCs and 25 PLTs) in the microvessel. However, not all the PLTs are firmly adhered onto the stenosed surface, and some of them can still move forward with the fluid. At $t = 15$, 11 cells (nine RBCs and two PLTs) move out of the microvessel, but 58 cells (18 RBCs and 40 PLTs) are in the microvessel. At $t = 20$, there are 38 cells (19 RBCs and 19 PLTs) flowing out of the microvessel, and 57 cells (18 RBCs and 39 PLTs) are still in the microvessel. At $t = 60$, 249 cells (95 RBCs and 154 PLTs) move out of the microvessel, and 60 cells (18 RBCs and 42 PLTs) are still in the microvessel. (b–d) Adhesion of a PLT. The PLT that is the same one as in Fig. 3(a) is observed from $t = 1$ to 13 with an interval of 0.5 , where an obvious adhesion is found at $t = 7.5$ (b). At this moment, the PLT forms the most bonds (c) and suffers from the largest adhesion force (d). Compared with Case A, the formed bonds cannot be maintained and are quickly dissociated, such that the microvessel is not blocked at all in the present case, and there are always about 60 cells in the microvessel after $t = 60$.

that the microvessel must be blocked if a RBC is rigid enough. Incidentally, the PLT deforms much less than the RBC, even when it is squeezed by the RBC in the stenosed region.

B. Adhesion force of PLTs

It is observed in Case A that the PLTs are firmly adhered onto the stenosed surface, which plays a critical role in thrombus formation. We halve the adhesion strength (Case B; see Fig. 4), to examine whether the microvessel is blocked under such a weak adhesion. Before the PLTs arrive at the stenosed region, i.e., $t < 5$, they exhibit the same behaviors as those in Case A, because the adhesion of PLTs does not happen yet (see Table II). After that, all the RBCs and most of the PLTs can pass through the stenosed region successfully. It is noted that totally five PLTs are adhered firmly until $t = 60$, but 154 PLTs move out of the microvessel. These five PLTs are adhered onto the downstream of the stenosed surface (see Ref. [39] for the video of Case B), which is consistent with the experimental observation by Nesbitt *et al.* [6]. Moreover, there are always about 60 cells in the microvessel from $t = 15$ to 60 , implying that the microvessel cannot be blocked even if the simulation is continued. When looking at a single PLT, we find that it quickly passes through the microvessel and cannot be firmly adhered onto the stenosed surface anymore.

There are still 35 bonds formed at about $t = 7.5$. However, these bonds cannot provide a high enough adhesion force to maintain them and are gradually broken subject to the shear force from the fluid flow and the attractive force from the RBCs. Until $t = 10$, all of them are completely broken, and the adhesion force decreases from a maximum value of about 4×10^4 (i.e., 83 pN) to 0. From $t = 7.5$ to 10 , the PLT is observed to roll on the stenosed surface, where the bond formation happens at the leading edge of the PLT, but the bond dissociation happens at the trailing edge. Because the speed of dissociating bonds is larger than that of forming new bonds, the final bond number has a decreasing trend. Therefore, it is clear that the PLT adhesion plays a crucial role in the microvessel blockage, that is, a weak adhesion cannot cause the microvessel blockage. This is quite useful for the prevention and treatment of thrombosis. It is worthy of note that a weak adhesion may be also achieved by other ways, such as reducing the rate of forming bonds or enhancing the rate of dissociating bonds.

C. Aggregation force between PLTs and RBCs

It is evaluated in Case A that at least 50 PLTs are required to capture a RBC in the stenosed region. We increase the interaction strength between PLTs and RBCs tenfold (Case

TABLE II. Comparisons of the number of PLTs and RBCs inside and outside the microvessel among Cases A–E.

Position	Type	Case	$t = 2$	$t = 5$	$t = 10$	$t = 15$	$t = 20$	$t = 25$	$t = 60$ ¹
Inside	RBC	A	4	9	18	21	21	24	–
		B	4	9	18	18	18	18	18
		C	4	9	18	22	28	33	–
		D	4	9	19	20	24	24	–
		E	7	16	17	17	17	17	18
	PLT	A	4	12	25	41	59	77	–
		B	4	12	25	40	39	45	42
		C	4	16	34	45	64	81	–
		D	4	12	25	43	59	77	–
		E	8	28	35	34	34	33	32
Outside	RBC	A	0	0	1	7	15	21	–
		B	0	0	1	9	19	28	95
		C	0	0	1	8	11	15	–
		D	0	0	1	8	14	23	–
		E	0	2	21	41	61	81	221
	PLT	A	0	0	0	0	0	0	–
		B	0	0	0	2	19	31	154
		C	0	0	0	7	8	8	–
		D	0	0	0	0	0	0	–
		E	0	0	27	62	99	132	369

¹The simulations are not run to $t = 60$ in Cases A, C, and D, and, hence, their cell numbers are not available.

C; see Fig. 5), to examine whether fewer PLTs are required to capture a RBC and whether the microvessel is blocked more easily in such a case. The RBCs are found to exhibit similar behaviors as Case A from $t = 2$ to 10 (see Table II). From $t = 15$ to 25, however, fewer RBCs flow out of the microvessel in Case C, and more RBCs are left in the microvessel. This implies that the microvessel is blocked more severely than that in Case A. Moreover, the PLTs have different behaviors from Case A from the beginning. In the present case, they are more concentrated around the RBCs, so that some of them are brought away by the RBCs and pass through the stenosis. Until $t = 25$, there are eight PLTs moving out the microvessel. Nevertheless, more PLTs stay in the microvessel than those in Case A, indicating again that the microvessel is blocked more severely.

When focusing on a pair of PLT and RBC, the PLT first moves into the microvessel before the RBC. At $t = 3.5$, the RBC enters into the interaction domain of the PLT, and they start to attract each other. At $t = 5$, their distance nearly reaches a minimum subject to the strong attraction. After that, a repulsion between them is present, which causes the RBC to sag near the PLT and forms a pit on its surface. This pit is more pronounced at $t = 7$, when the cell pair are right located at the narrowest region of the microvessel. Subsequently, their distance increases due to the strong repulsion, and because of the expansion of the microvessel after the stenosed region, such that their mutual attraction comes back again from $t = 7.5$. Hence, the RBC pit gradually becomes shallow, for example, at $t = 9$. At around $t = 12$, both the RBC and the PLT move out of the microvessel. It is found during the whole process that the RBC brings the PLT together with it to move out of the microvessel, due to a strong aggregation force. From this viewpoint, the strong aggregation does not aggravate the microvessel blockage, because fewer PLTs will be adhered if the microvessel is wide enough in diameter.

To sum up, the aggregation between PLTs and RBCs may have two different effects on thrombus formation. When the blockage is not severe or the microvessel is quite wide, the strong aggregation allows the RBCs to bring the PLTs away to pass through the stenosis together. Thus, the PLT adhesion does not happen so that the blockage is not aggravated. When the blockage has been severe, the strong aggregation causes more RBCs captured onto the stenosed region by the fewer PLTs, which makes the blockage grow worse and even the microvessel is completely blocked. Thus, it is meaningful to find a criterion for what marks the transition between a severe stenosis in which increasing aggregation strength makes it worse, as opposed to one in which the increased aggregation strength allows the RBCs to bring the platelets away. However, it is not easy to find such a criterion, which depends on not only the RBC-PLT aggregation strength but also the degree of the microvessel stenosis, thus requiring a large amount of computational cost. In the near future, we may put more efforts on this criterion by considering the different configurations of the microvessels, different sizes of the stenoses, and the different RBC-PLT aggregation strengths.

D. Deformation force of RBCs

It is stated in Case A that the RBC deformability allows it to pass through the stenosis, which can relieve the microvessel blockage. We reduce the RBC shear modulus tenfold (Case D; see Fig. 6), to examine whether the microvessel is still blocked. No RBCs are found to flow more easily through the stenosed region due to the high deformability, and all the PLTs still cannot pass through the stenosed region. Hence, both the RBCs and PLTs have a similar number as those in Case A at each time instant (see Table II), implying that the RBC deformability has no significant effect on the microvessel blockage, even if its shear modulus is changed 10

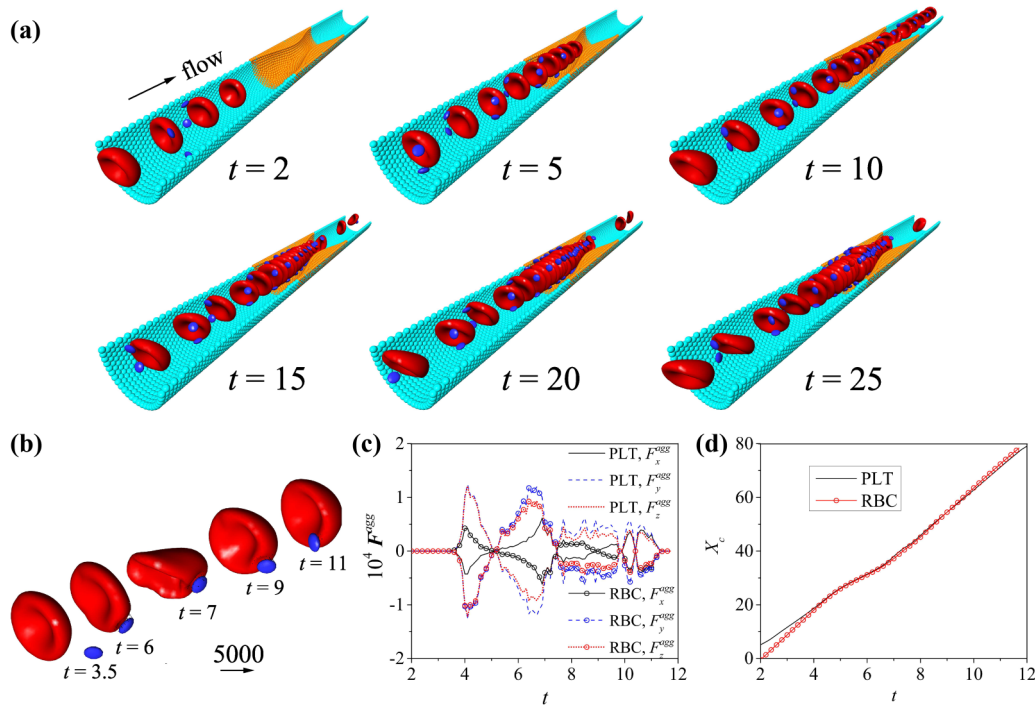


FIG. 5. Effect of the interaction strength between PLTs and RBCs (Case C; see Ref. [39] for the video of Case C). (a) Six snapshots of PLTs and RBCs under a strong interaction strength. At $t = 2$, there are eight cells (four RBCs and four PLTs) flowing into the microvessel. At $t = 5$, 25 cells (nine RBCs and 16 PLTs) are in the microvessel, and the leading RBC arrives at the stenosed region. At $t = 10$, there is a RBC flowing out of the microvessel, and 52 cells (18 RBCs and 34 PLTs) are still in the microvessel. However, not all the PLTs are firmly adhered onto the stenosed surface, and some of them can still move forward with the fluid. At $t = 15$, 15 cells (eight RBCs and seven PLTs) move out of the microvessel, but 67 cells (22 RBCs and 45 PLTs) are in the microvessel. At $t = 20$, there are 19 cells (11 RBCs and eight PLTs) flowing out of the microvessel, and 92 cells (28 RBCs and 64 PLTs) are still in the microvessel. At $t = 25$, 23 cells (15 RBCs and eight PLTs) move out of the microvessel, and there are 114 cells (33 RBCs and 81 PLTs) still in the microvessel, 13 more than Case A. This implies that the microvessel is blocked more severely than that in Case A. A same pair of RBC and PLT in Fig. 3(d) are considered for comparison (b–d). The aggregation force between them starts to appear at about $t = 3.5$ and disappears at about $t = 12$ (b). During this time interval, their resultant forces \mathbf{F}^{agg} are still equal in magnitude and opposite in direction, but they no longer have a unique increasing or decreasing trend anymore (c). Moreover, the PLT is dragged by the RBC to pass through the stenosed region, and finally moves out of the microvessel together with the RBC (d).

times. It is also found that the RBCs indeed deform more in the present case, with a smaller average asphericity. That is, the RBCs deform to be more round in Case D than Case A. However, their average velocities are similar in Case D and Case A, and this is the reason why the RBC deformability has no significant effect on the microvessel blockage. In our previous studies [51], the RBC was found to have a larger velocity in a nonstenosed microvessel if its deformability is higher, because it is more compliant to the fluid flow. However, this conclusion is not straightforward anymore in the very stenosed microvessel. Before $t = 10$, the cells have not yet arrived at the stenosed region, and the RBCs indeed have the larger average velocity than those in Case A, similarly with in the nonstenosed microvessel. However, when the cells move into the stenosed region, they instead have a smaller average velocity until $t = 17.5$. It is noted during this period that the RBCs have a similar average asphericity as in Case D and Case A. After $t = 17.5$, the average asphericity of the RBCs becomes smaller in Case D than that in Case A again, and the corresponding average velocity is larger again. It is inferred that the stenosed region is so narrow that it squeezes the rigid RBCs with the similar deformation to the soft RBCs

in order to pass through this stenosed region. Therefore, the high deformability of RBCs can increase the flow velocity and thus improve the microvessel blockage. However, if the microvessel is blocked severely or narrow enough, this effect is not obvious or even negligible.

IV. CONCLUSIONS

The process of thrombus formation has been extensively studied in the past several decades, and much effort has been spent characterizing the biological and biochemical aspects of clotting. In the recent decade, more and more evidence has shown that the function and physiology of blood cells and plasma proteins relevant in formation process are mechanically, as well as biologically, regulated [2], such as PLT adhesion, RBC deformation, etc. The mechanical factors cause the blood components to exhibit different behaviors in the biochemical and biomechanical aspects from the macro to cellular to molecular scale. These behaviors are in turn involved and play important role in the process of thrombus formation.

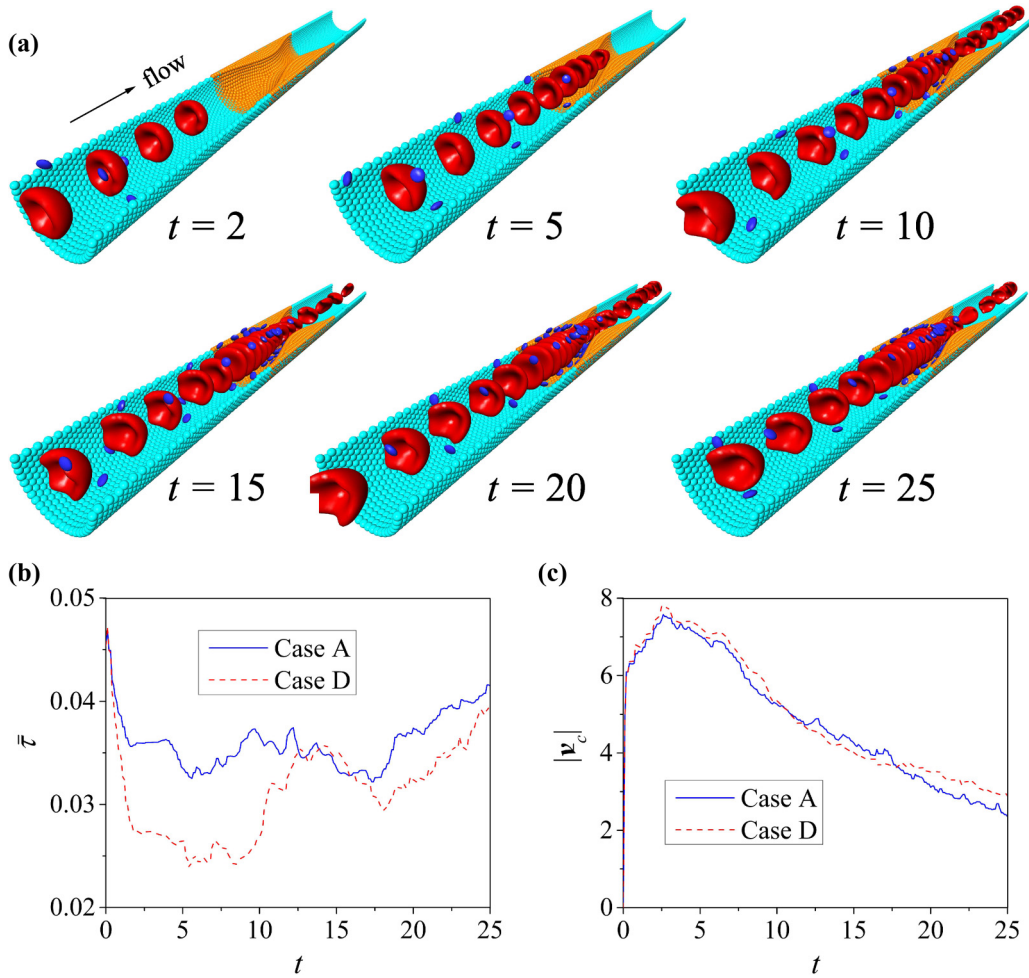


FIG. 6. Effect of the deformability of RBCs (Case D; see Ref. [39] for the video of Case D). (a) Six snapshots of PLTs and RBCs that have the high deformability. At $t = 2$, there are eight cells (four RBCs and four PLTs) in the microvessel, while at $t = 5$, 21 cells (nine RBCs and 12 PLTs) are in the microvessel. At $t = 10$, there is also a RBC flowing out of the microvessel, and 44 cells (19 RBCs and 25 PLTs) are still in the microvessel. At $t = 15$, eight RBCs move out of the microvessel, but 63 cells (20 RBCs and 43 PLTs) are in the microvessel. At $t = 20$, there are 14 RBCs flowing out of the microvessel, and 83 cells (24 RBCs and 59 PLTs) are still in the microvessel. At $t = 25$, 23 RBCs move out of the microvessel, and 101 cells (24 RBCs and 77 PLTs) are still in the microvessel. At each time instant, the RBCs and PLTs have the similar numbers with those in Case A, implying that the RBC deformability has no significant effect on the microvessel blockage. To compare the RBC deformation between Case A and Case D, the average asphericity $\bar{\alpha}$ is calculated by averaging over all the RBCs in the microvessel at each time instant (b). It has a maximum variation of 0.0233 in Case D but 0.0148 in Case A. The movement of all the RBCs is described by the magnitude $|\bar{v}_c|$ of the average velocity of all the RBCs at each time instant (c).

Here we performed direct simulations of the process of thrombus formation at a cellular scale, to study the biomechanics in this process, especially including the PLT adhesion and aggregation, the RBC deformation and aggregation, and the interaction between the PLT and RBC. In fact, it has been quite difficult to reproduce such a process of thrombus formation in both experiments and simulations so far, despite significant progress made in the recent decade. Experimental observations are limited by the reliability of measurements and the complexity of blood flow around the thrombus [3]. Numerical modeling faces also great challenges due to the polydisperse feature of blood components and their multiple biochemical and biomechanical behaviors [4,5]. We used a mesoscale numerical method, SDPD-IBM, which allows us not only to simulate a large number of RBCs and PLTs, compared with the microscale numerical methods, but also to

implement the adhesion and aggregation binding of cells more easily, compared with the macroscale numerical methods.

We mainly answered the following critical questions about thrombus formation in the present work. Can the microvessel still be blocked if the PLTs do not exhibit the firm adhesion or if the RBCs deform more easily? Is the microvessel blocked more severely if the interaction between the RBCs and PLTs becomes stronger? The simulation results showed that when the adhesion strength of PLTs is reduced twice (Case B), most of the PLTs cannot be firmly adhered onto the stenosed surface, and the RBCs are not aggregated in the stenosed region. As a result, the microvessel is not blocked anymore. This implies that the PLT adhesion has a direct and crucial effect on the microvessel blockage. When the RBC deformability is enhanced 10 times (Case D), the microvessel blockage has not been reduced significantly and even is almost same as the situ-

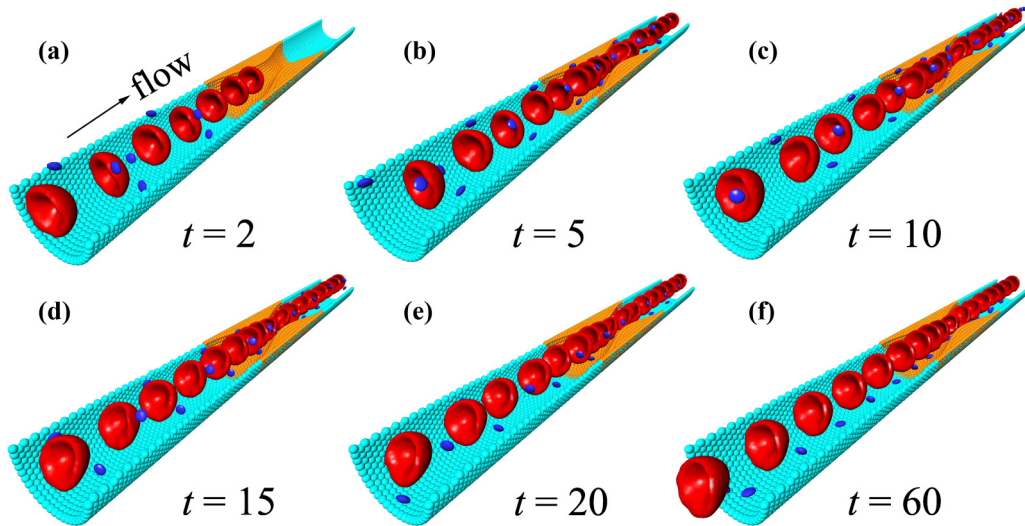


FIG. 7. Effect of the flow velocity (Case E; see Ref. [39] for the video of Case E). At $t = 2$ (a), there are 15 cells (seven RBCs and eight PLTs) flowing in the microvessel. At $t = 5$ (b), there are two RBCs flowing out of the microvessel, and 44 cells (16 RBCs and 28 PLTs) are still in the microvessel. At $t = 10$ (c), 48 cells (21 RBCs and 27 PLTs) move out of the microvessel, and 52 cells (17 RBCs and 35 PLTs) are in the microvessel. At $t = 15$ (d), there are 103 cells (41 RBCs and 62 PLTs) flowing out of the microvessel, and 51 cells (17 RBCs and 34 PLTs) are in the microvessel. At $t = 20$ (e), there are 160 cells (61 RBCs and 99 PLTs) flowing out of the microvessel, and 51 cells (17 RBCs and 34 PLTs) are still in the microvessel. At $t = 60$ (f), 590 cells (221 RBCs and 369 PLTs) move out of the microvessel, and 50 cells (18 RBCs and 32 PLTs) are still in the microvessel. It is found that the number of cells in the microvessel is not changed obviously, about 50 cells from $t = 10$, implying that the microvessel is not blocked any longer.

ation without enhancing the deformability. This is because the average velocity of the RBCs does not increase significantly in the very stenosed microvessel, which is different with the case of RBCs in the nonstenosed microvessel. When the aggregation strength between the RBCs and PLTs is enhanced 10 times (Case C), the microvessel blockage may be or may be not aggravated. If the blockage is not severe, the strong aggregation enables the RBCs to bring away the PLTs to pass through the stenosis together, such that the PLT adhesion does not happen and the blockage is thus not aggravated. However, if the blockage has been severe, the strong aggregation causes more RBCs to be captured onto the stenosed region by the PLTs, such that the blockage gets worse and worse.

The above effects about the PLT adhesion, the RBC-PLT interaction, and the RBC deformability were analyzed individually by defining three dimensionless numbers, Ca_A , Ca_I , and Ca_S (see the Appendix), respectively. In short, increasing Ca_A can directly reduce the microvessel blockage; decreasing Ca_I may lead to the blockage becoming worse and worse, but may also have no significant influences (i.e., increasing Ca_I may reduce the microvessel blockage); and decreasing Ca_S does not aggravate the microvessel blockage significantly (i.e., increasing Ca_S does not reduce the microvessel blockage significantly). Therefore, if all of these three dimensionless numbers are increased at the same time, it is predictable that this may be the most efficient way to reduce the microvessel blockage, compared with any individual way. This prediction is confirmed by Case E (see Fig. 7), where the the velocity of blood flow is doubled, leading to Ca_A , Ca_I , and Ca_S increased twice simultaneously. There are 590 cells (249 cells in Case B) moving out the microvessel until $t = 60$, and about 50 cells (60 cells in Case B) are still in the microvessel (see Table II). It is clear that the cells move more fluidly than those in Case B,

and the microvessel is not blocked at all. This result implies that maintaining high-rate blood flow plays a crucial role in the prevention and treatment of thrombosis, which is even more effective than antiplatelet or anticoagulant drugs. Although it is not easy and may be dangerous to suddenly elevate the rate of blood flow clinically, some long-term measures are also effective in practice, for example, doing more exercise for speeding up the blood flow, eating light foods to decrease the blood viscosity, receiving massage to increase the blood circulation, and even taking some blood-activating drugs, etc. Therefore, keep in mind that maintaining high-rate blood flow may be one of the most effective ways to prevent and treat thrombosis.

ACKNOWLEDGMENTS

The authors acknowledge financial support from the National Natural Science Foundation of China under Project No. 11502094, and the Jilin Province Natural Science Foundation of China under Project No. 20180520024JH. The authors would also like to acknowledge all the support from the School of Mathematics at Jilin University of China.

APPENDIX: MATHEMATICAL MODELS

1. SDPD-IBM

The cells (RBCs and PLTs) in Fig. 1 are filled with cytoplasm fluid and suspended in the medium fluid. Both fluids are assumed to be incompressible and Newtonian, and the flow is isothermal due to the slow to moderate flow velocity. The cell membrane is regarded as a curved surface immersed in both fluids, i.e., an immersed boundary (IB). Therefore, the

motion of the fluids inside and outside the cells is governed by Navier-Stokes (NS) equations [52],

$$\nabla \cdot \mathbf{v} = 0, \quad (\text{A1})$$

$$\rho \frac{d\mathbf{v}}{dt} = -\nabla P + \eta \nabla^2 \mathbf{v} + \rho \mathbf{g} + \mathbf{f}, \quad (\text{A2})$$

where \mathbf{v} , ρ , and P are the velocity, density, and pressure fields of a fluid, respectively, t is the time, η is the shear viscosity of fluid, and \mathbf{g} is the gravity that drives the fluid flow, \mathbf{f} accounts for the singular force acting on the fluid due to the existence of an IB (or a cell), given by

$$\mathbf{f}(\mathbf{x}, t) = \int_{\Gamma} \mathbf{F}_d(r, s, t) \delta[\mathbf{x} - \mathbf{X}(r, s, t)] dr ds, \quad (\text{A3})$$

$$\frac{d\mathbf{X}}{dt} = \mathbf{v}(\mathbf{X}, t) = \int_{\Omega} \mathbf{v}(\mathbf{x}, t) \delta[\mathbf{x} - \mathbf{X}(r, s, t)] d\mathbf{x}, \quad (\text{A4})$$

and Γ and Ω are the IB and the whole domain, respectively. Note that (r, s) is a curvilinear coordinate attached to the IB to label a Lagrangian point on it, $\mathbf{X}(r, s, t)$ is the position of the Lagrangian point (r, s) at time t , and \mathbf{x} is a spatial point in the Eulerian system. Hence, $\mathbf{v}(\mathbf{x}, t)$ refers to the velocity of whatever Lagrangian point happens to be at Eulerian position \mathbf{x} at time t , while $\mathbf{v}(\mathbf{X}, t)$ refers to the velocity of the Lagrangian point (r, s) at time t . $\mathbf{F}_d(r, s, t)$ is the force density on the unit surface area of IB at the point (r, s) .

In the SDPD framework, the whole domain is represented by a set of discrete particles, and each of them is associated with physical properties, such as mass, velocity, density, etc. An arbitrary field function $f(\mathbf{x}_i)$ and its derivative $\nabla f(\mathbf{x}_i)$ are interpolated by a kernel function within the compact support domain and can be written as [53]

$$f(\mathbf{x}_i) \approx \sum_j \frac{m_j}{\rho_j} f(\mathbf{x}_j) W_{ij}, \quad (\text{A5})$$

$$\nabla f(\mathbf{x}_i) \approx \sum_j \frac{m_j}{\rho_j} f(\mathbf{x}_j) \nabla W_{ij}, \quad (\text{A6})$$

where \mathbf{x}_i is the position of particle i , m_j and ρ_j are the mass and density of particle j , and W_{ij} is the kernel function.

By substituting the SDPD approximations for a function and its derivative in Eqs. (A5) and (A6) into the governing equations (A1)–(A4), we have the SDPD-IBM formulation in Eqs. (1)–(4),

$$\begin{aligned} d\mathbf{x}_i &= \mathbf{v}_i dt, \\ m d\mathbf{v}_i &= \mathbf{F}_C dt + \mathbf{F}_D dt + \mathbf{F}_R + \mathbf{F}_G dt + \mathbf{F}_B dt, \\ \mathbf{F}_B &= \sum_k \beta_{ik} (\mathbf{F}_k^{def} + \mathbf{F}_k^{agg} + \mathbf{F}_k^{adh}), \\ \frac{d\mathbf{X}_k}{dt} &= \sum_i \beta_{ik} \mathbf{v}_i. \end{aligned} \quad (\text{A7})$$

Here the forces are expressed as follows [34,53]:

$$\begin{aligned} \mathbf{F}_C &= \sum_j \alpha_{ij} \mathbf{x}_{ij}, \quad \mathbf{F}_D = - \sum_j \gamma_{ij} [\mathbf{v}_{ij} + (\mathbf{e}_{ij} \cdot \mathbf{v}_{ij}) \mathbf{e}_{ij}], \\ \mathbf{F}_R &= \sum_j A_{ij} \widehat{\mathbf{W}}_{ij} \cdot \mathbf{e}_{ij}, \quad \mathbf{F}_G = m\mathbf{g}, \end{aligned} \quad (\text{A8})$$

where $\mathbf{v}_{ij} = \mathbf{v}_i - \mathbf{v}_j$, $\mathbf{e}_{ij} = \mathbf{x}_{ij}/x_{ij}$, $x_{ij} = |\mathbf{x}_{ij}|$, and $\mathbf{x}_{ij} = \mathbf{x}_i - \mathbf{x}_j$. $d\mathbf{W}_{ij}$ is a 3×3 matrix for the 3D case, constructed by independent increments of the Wiener process, and $\widehat{d\mathbf{W}}_{ij}$ is its symmetric part defined as

$$\widehat{d\mathbf{W}}_{ij} = \frac{1}{2} (d\mathbf{W}_{ij} + d\mathbf{W}_{ij}^T), \quad (\text{A9})$$

where $d\mathbf{W}_{ij}^T$ is the transposition of $d\mathbf{W}_{ij}$. The coefficients α_{ij} , γ_{ij} , A_{ij} , and β_{ik} are given by

$$\begin{aligned} \alpha_{ij} &= \left(\frac{P_i}{d_i^2} + \frac{P_j}{d_j^2} \right) F_{ij}, \quad \gamma_{ij} = \frac{5\eta}{3} \frac{F_{ij}}{d_i d_j}, \\ A_{ij} &= \left[\frac{20\eta k_B T}{3} \frac{F_{ij}}{d_i d_j} \right]^{\frac{1}{2}}, \quad \beta_{ik} = \frac{W_{ik}}{d_i}, \end{aligned} \quad (\text{A10})$$

where P_i and $d_i = \rho_i/m$ are the pressure and number density, respectively, of the fluid particle i , $k_B T$ is the Boltzmann temperature (actually, the specific kinetic energy, to be kept constant), and F_{ij} is the geometrical function defined as

$$F_{ij} = -\frac{1}{x_{ij}} \frac{dW_{ij}}{dx_{ij}}. \quad (\text{A11})$$

2. Cell deformation model

To formulate the membrane forces, each cell membrane is modeled as a triangular network, associated with three types of potential energies: deformation, aggregation, and adhesion energies U_{def} , U_{agg} , and U_{adh} , respectively. Hence, the membrane forces are defined as

$$\mathbf{F}_k^{sub} = -\frac{\partial U_{sub}}{\partial \mathbf{X}_k}, \quad (\text{A12})$$

where the script *sub* refers to *def*, *agg*, and *adh*, respectively. Note that the energy dissipation of the membrane is not taken into account for simplicity, and this should be justified when caring less about the cell relaxation.

The deformation energy U_{def} is composed of the four types of energies: (1) the in-plane energy for describing the stretching deformation, (2) the bending energy for describing the bending deformation, (3) the area-restraint energy for conserving the membrane area, and (4) the volume-restraint energy for conserving the cell volume [54,55],

$$U_{def} = U_s + U_b + U_a + U_v, \quad (\text{A13})$$

It is assumed that the triangular network are connected by the wormlike springs, i.e., the triangular edge is modeled as the wormlike spring, and hence the in-plane energy U_s is given by

$$U_s = \sum_{j=1, \dots, N_s} \left(\frac{k_B T L_j}{4p_j} \frac{3s_j^2 - 2s_j^3}{1 - s_j} + \frac{\chi_j}{s_j L_j} \right), \quad (\text{A14})$$

where $s_j = l_j/L_j$, l_j , and L_j are the current and maximum length of the spring j , p_j is the persistence length, χ_j is a repulsive coefficient, and N_s is the number of springs. The bending energy is defined as

$$U_b = \sum_{j=1, \dots, N_s} K_B [1 - \cos(\theta_j - \theta_j^d)], \quad (\text{A15})$$

where K_B is the bending coefficient, and θ_j and θ_j^d are the current and desired angles between two adjacent triangles having the common edge j . The area-restraint energy consists of the restraint energies from the whole cell area and each triangle area,

$$U_a = \frac{K_{AG}(A - A^d)^2}{2A^d} + \sum_{j=1, \dots, N_t} \frac{K_{AL}(A_j - A_j^d)^2}{2A_j^d}, \quad (\text{A16})$$

where K_{AG} and K_{AL} are the global and local area restraint constants, A and A_j are the areas of the whole cell and triangle j , A^d and A_j^d are the corresponding desired areas, and N_t is the number of triangles on the cell membrane. Similarly, the volume-restraint energy is defined as

$$U_v = \frac{K_V(V - V^d)^2}{2V^d}, \quad (\text{A17})$$

where K_V is the volume restraint constant, and V and V^d are the current and desired volumes of cell.

3. Cell aggregation model

So far, there are two theoretical descriptions of cell aggregation: the bridging model [56] and the depletion model [57]. Both models suggest that the cells tend to aggregate when the attractive force between them is larger than the repulsive force, and the repulsive force is generated by electrostatic repulsion, membrane shearing, and membrane bending. For the attractive force, however, the former model assumes that it is attributed to the bridging of macromolecules between the cells, such as fibrinogen or dextran. The latter model proposes that it is due to the existence of the polymer depletion layer between the cells, accompanied by a decrease of the osmotic pressure. Mathematically, these two models are so complex that they are not widely used in numerical simulations to describe the cell aggregation [58]. For simplicity, Liu *et al.* [59] proposed the Morse potential model, in which a Morse potential function is employed to fit the total aggregation energy between the cells [60],

$$U_{agg} = \sum_{m=1, \dots, N_t} \phi(r_{mm'}) (\mathbf{n}_m \cdot \mathbf{k}_m) (\mathbf{n}_{m'} \cdot \mathbf{k}_{m'}) A_m, \quad (\text{A18})$$

where the subscripts m and m' refer to the triangles m and m' of the two respective cells, \mathbf{n} is the outward unit normal vector of the triangle, \mathbf{k} is the unit vector in the direction parallel to the line joining the centers of two interacting cells, A_m is the area of the triangle m , and N_t is the number of triangles. The term $\phi(r_{mm'})$ is the so-called Morse potential function, describing the interaction energy between two unit flat planes, given by [59]

$$\phi(r_{mm'}) = E_l [e^{2\beta(r_0 - r_{mm'})} - 2e^{\beta(r_0 - r_{mm'})}], \quad (\text{A19})$$

where E_l is the surface energy, β is a scaling factor, r_0 is the zero force separation, and $r_{mm'}$ is the local distance between two facing unit flat planes. The terms $\mathbf{n}_m \cdot \mathbf{k}_m$ and $\mathbf{n}_{m'} \cdot \mathbf{k}_{m'}$ are added to handle the interaction between two curved surfaces instead of flat planes [58]. Based on this aggregation energy, the aggregation force behaves as a weak attractive force at a far intercellular distance, $r_{mm'} > r_0$, but a strong repulsive force at a near intercellular distance, $r_{mm'} < r_0$. It is found that

the Morse potential model, in fact, cannot reflect any biological or physical meanings of the cell aggregation. It is just a mathematical formula to fit the experimental aggregation energy, and then differentiating the aggregation energy gives the adhesion force.

4. PLT adhesion model

The adhesion potential energy U_{adh} is described by a stochastic receptor-ligand binding kinetics, given by

$$U_{adh} = \frac{1}{2} \sum_{m=1, \dots, N_b} E_A (x_m - \lambda)^2, \quad (\text{A20})$$

where N_b is number of bonds; x_m , λ , and E_A are length, equilibrium length, and strength of a formed bond, respectively. The formation and dissociation of a bond is modeled by stochastic receptor-ligand binding kinetics, in which a forming probability p_f and a rupturing probability p_r are introduced as

$$p_f = 1 - \exp(-k_f \Delta t) \quad (\text{A21})$$

and

$$p_r = 1 - \exp(-k_r \Delta t), \quad (\text{A22})$$

where Δt is the simulation time step. k_f and k_r are the rates of forming and rupturing a bond, defined as

$$k_f = k_f^0 \exp\left[-\frac{\sigma_f(x_m - \lambda)^2}{2k_b T}\right] \quad (\text{A23})$$

and

$$k_r = k_r^0 \exp\left[\frac{\sigma_r(x_m - \lambda)^2}{2k_b T}\right], \quad (\text{A24})$$

where k_f^0 , k_r^0 , σ_f , and σ_r are four constants, and $k_b T$ is the Boltzmann temperature. k_f^0 and k_r^0 are the unstressed forming and rupturing rates of bonds at the equilibrium distance; σ_f and σ_r are the forming and rupturing strengths within a given distance. If a bond is formed, two conditions must be satisfied: (1) $x_m < l_f$, where l_f is the maximum distance allowing formation of a bond, and (2) $p_f > \xi$, where ξ is a random number with uniform distribution in $[0, 1]$. If an existing bond is ruptured, one of the two following conditions is satisfied: (1) $x_m \geq l_r$, where l_r is the minimum distance for rupturing a bond, or (2) $p_r > \zeta$, where ζ is another random number with uniform distribution. This stochastic adhesion model takes into account the dynamic effects of the protein receptors and ligands by mathematically controlling the model parameters; for example, the average length of vWF can be controlled by the equilibrium length λ of a bond. However, if one wants to study the detailed vWF dynamics, the model parameters may not be constants and determined only with difficulty. An alternative approach may be more suitable that the vWF is modeled as a separate chain, as studied in the work of Rack *et al.* [61].

5. Nondimensionalization

To perform the nondimensionalization of theoretical models, three basic characteristic quantities are chosen: using the cutoff radius of SDPD as the basic characteristic length l' ,

the mass of a fluid particle as the basic characteristic mass m' , and the Boltzmann temperature of system as the basic characteristic energy ε' . In the present work, we set $l' = 2 \mu\text{m}$, $m' = 1.0 \times 10^{-15} \text{ kg}$, and $\varepsilon' = 4.142 \times 10^{-21} \text{ J}$. Other characteristic quantities can be derived from these three basic ones, e.g., the characteristic time $t' = l' \sqrt{m'/\varepsilon'}$ (see Table I). The physical variables are now scaled with respect to the characteristic quantities, for example,

$$\hat{\mathbf{x}}_i = \frac{\mathbf{x}_i}{l'}, \quad \hat{\mathbf{v}}_i = \frac{\mathbf{v}_i}{\sqrt{\varepsilon'/m'}}, \quad \hat{t} = \frac{t}{l' \sqrt{m'/\varepsilon'}}, \quad (\text{A25})$$

and Eq. (1) can be scaled into

$$d(\hat{\mathbf{x}}_i \hat{t}) = (\hat{\mathbf{v}}_i \sqrt{\varepsilon'/m'}) d(\hat{t} \sqrt{m'/\varepsilon'}), \quad (\text{A26})$$

and canceling out the same quantities from both sides gives

$$d\hat{\mathbf{x}}_i = \hat{\mathbf{v}}_i d\hat{t}. \quad (\text{A27})$$

It is found that the nondimensional form of the SDPD-IBM formulation is the same as its dimensional form, and thus we omit the hat ($\hat{\cdot}$) of the nondimensional variables in the present work. There are several important dimensionless groups associated with the SDPD-IBM model, listed below, where the subscript “0” refers to the typical values of physical quantities in a given problem:

1. Mach number Ma : describes the relative importance of flow inertia to sound speed,

$$\text{Ma} = \frac{v_0}{c}. \quad (\text{A28})$$

Because the SDPD-IBM uses the artificial sound speed to control the fluid compressibility, we always let $\text{Ma} \leq 0.1$ in the present work.

2. Reynolds number Re : describes the relative importance of flow inertia to viscosity,

$$\text{Re} = \frac{\rho_0 v_0 l_0}{\eta_0}. \quad (\text{A29})$$

In the present work, we let $\text{Re} \leq 0.5$, and it has been found that the Reynolds number has a slight effect on the cell behaviors when $\text{Re} \leq 1$.

3. Froude number Fr : describes the relative importance of flow inertia to gravity,

$$\text{Fr} = \frac{v_0}{\sqrt{g_0 l_0}}. \quad (\text{A30})$$

This number depends on the externally applied force used to drive the fluid flow.

4. Capillary number Ca_A of the adhesion of PLTs: describes the relative importance of viscous force to the PLT adhesion force,

$$\text{Ca}_A = \frac{\eta_0 v_0}{\tilde{E}_A}, \quad (\text{A31})$$

where \tilde{E}_A is the adhesion strength of PLTs.

5. Capillary number Ca_I of the aggregation between PLTs and RBCs: describes the relative importance of viscous force to the aggregation force between PLTs and RBCs,

$$\text{Ca}_I = \frac{\eta_0 v_0}{\hat{E}_I}, \quad (\text{A32})$$

where \hat{E}_I is the aggregation strength between PLTs and RBCs.

6. Capillary number Ca_S of the deformation of RBCs: describes the relative importance of viscous force to the RBC deformation force,

$$\text{Ca}_S = \frac{\eta_0 v_0}{E_S}, \quad (\text{A33})$$

where E_S is the shear modulus of RBCs.

6. Numerical methods

The velocity-Verlet algorithm is used to solve governing equations (1)–(4), and its procedures are given as follows [42,43]:

Step 1: Update coordinates of membrane particles

$$\mathbf{X}_k^{n+1} = \mathbf{X}_k^n + \Delta t \sum_i \beta_{ik}^n \mathbf{v}_i^n, \quad (\text{A34})$$

where the superscript n refers to the n th simulation step, and Δt is the time step;

Step 2: Update coordinates of fluid particles

$$\mathbf{x}_i^{n+1} = \mathbf{x}_i^n + \Delta t \mathbf{v}_i^n + \frac{\Delta t^2}{2m} \mathbf{F}_T^n, \quad (\text{A35})$$

where \mathbf{F}_T^n is the total force;

Step 3: Predict velocities of fluid particles

$$\tilde{\mathbf{v}}_i^{n+1} = \mathbf{v}_i^n + \omega \frac{\Delta t}{m} \mathbf{F}_T^n, \quad (\text{A36})$$

where ω is an empirical factor with the optimal value of 0.65 [42];

Step 4: Calculate all types of forces

$$\mathbf{F}_T^{n+1} = \mathbf{F}_C + \mathbf{F}_D + \mathbf{F}_R/\Delta t + \mathbf{F}_G + \mathbf{F}_B; \quad (\text{A37})$$

Step 5: Correct the velocities of fluid particles

$$\mathbf{v}_i^{n+1} = \tilde{\mathbf{v}}_i^{n+1} + \frac{\Delta t}{2m} \mathbf{F}_T^{n+1}. \quad (\text{A38})$$

After these five steps, the coordinates and velocities of the fluid particles are obtained, as well as the coordinates of the membrane particles of the RBCs and PLTs.

-
- [1] World Health Organization, World health statistics 2019: Monitoring health for the SDGs, sustainable development goals, Tech. Rep., Geneva, 2019.
- [2] R. Tran, D. R. Myers, J. Ciciliano, E. L. T. Hardy, Y. Sakurai, B. Ahn, Y. Qiu, R. G. Mannino, M. E. Fay, and W. A. Lam,

- Biomechanics of haemostasis and thrombosis in health and disease: From the macro- to molecular scale, *J. Cell. Mol. Med.* **17**, 579 (2013).
- [3] A. S. Popel and P. C. Johnson, Microcirculation and hemorheology, *Ann. Rev. Fluid Mech.* **37**, 43 (2005).

- [4] P. Balogh and P. Bagchi, A computational approach to modeling cellular-scale blood flow in complex geometry, *J. Comput. Phys.* **334**, 280 (2017).
- [5] H. Hosseinzadegan and D. K. Tafti, Modeling thrombus formation and growth, *Biotech. Bioeng.* **114**, 2154 (2017).
- [6] W. S. Nesbitt, E. Westein, F. J. Tovar-Lopez, E. Tolouei, A. Mitchell, J. Fu, J. Carberry, A. Fouras, and S. P. Jackson, A shear gradient-dependent platelet aggregation mechanism drives thrombus formation, *Nat. Med.* **15**, 665 (2009).
- [7] Z. Chen, J. Lu, C. Zhang, I. Hsia, X. Yu, L. Marecki, E. Marecki, M. Asmani, S. Jain, S. Neelamegham, and R. Zhao, Microclot array elastometry for integrated measurement of thrombus formation and clot biomechanics under fluid shear, *Nat. Commun.* **10**, 2051 (2019).
- [8] E. Mihalko and A. C. Brown, Clot structure and implications for bleeding and thrombosis, *Semin. Thromb. Hemost.* **46**, 96 (2020).
- [9] A. L. Fogelson and K. B. Neeves, Fluid mechanics of blood clot formation, *Ann. Rev. Fluid. Mech.* **47**, 377 (2015).
- [10] N. Mackman, Triggers, targets and treatments for thrombosis, *Nature (London)* **451**, 914 (2008).
- [11] W. A. Lam, O. Chaudhuri, A. Crow, K. D. Webster, A. Kita, J. Huang, and D. A. Fletcher, Mechanics and contraction dynamics of single platelets and implications for clot stiffening, *Nat. Mater.* **10**, 61 (2011).
- [12] J.-P. Collet, H. Shuman, R. E. Ledger, S. Lee, and J. W. Weisel, The elasticity of an individual fibrin fiber in a clot, *Proc. Natl. Acad. Sci. USA* **102**, 9133 (2005).
- [13] A. E. X. Brown, R. I. Litvinov, D. E. Discher, P. K. Purohit, and J. W. Weisel, Multiscale mechanics of fibrin polymer: Gel stretching with protein unfolding and loss of water, *Science* **325**, 741 (2009).
- [14] J. Rivera, M. L. Lozano, L. Navarro-Núñez, and V. Vicente, Platelet receptors and signaling in the dynamics of thrombus formation, *Haematologica* **94**, 700 (2009).
- [15] K. M. Dayananda, I. Singh, N. Mondal, and S. Neelamegham, von Willebrand factor self-association on platelet GpIb α under hydrodynamic shear: Effect on shear-induced platelet activation, *Blood* **116**, 3990 (2010).
- [16] S. P. Jackson, W. S. Nesbitt, and S. Kulkarni, Signaling events underlying thrombus formation, *J. Throm. Haem.* **1**, 1602 (2010).
- [17] F. Gaertner, Z. Ahmad, G. Rosenberger, S. Fan, L. Nicolai, B. Busch, G. Yavuz, M. Luckner, H. Ishikawa-Ankerhold, R. Hennel, *et al.*, Migrating platelets are mechano-scavengers that collect and bundle bacteria, *Cell* **171**, 1368 (2017).
- [18] Y. Zhang, Y. Qiu, A. T. Blanchard, Y. Chang, J. M. Brockman, V. P. Ma, W. A. Lam, and K. Salaita, Platelet integrins exhibit anisotropic mechanosensing and harness piconewton forces to mediate platelet aggregation, *Proc. Natl. Acad. Sci. USA* **115**, 325 (2018).
- [19] S. P. Jackson, The growing complexity of platelet aggregation, *Blood* **109**, 5087 (2007).
- [20] M. D. Giovanni Davì and M. D. Carlo Patrono, Platelet activation and atherothrombosis, *New Engl. J. Med.* **357**, 2482 (2007).
- [21] S. M. de Witt, F. Swieringa, R. Cavill, M. M. Lamers, R. Van Kruchten, T. Mastenbroek, C. Baaten, S. Coort, N. Pugh, A. Schulz, *et al.*, Identification of platelet function defects by multi-parameter assessment of thrombus formation, *Nat. Commun.* **5**, 4257 (2014).
- [22] W. Bergmeier, C. L. Piffath, T. Goerge, S. M. Cifuni, Z. M. Ruggeri, J. Ware, and D. D. Wagner, The role of platelet adhesion receptor GPIb α far exceeds that of its main ligand, von Willebrand factor, in arterial thrombosis, *Proc. Natl. Acad. Sci. USA* **103**, 16900 (2006).
- [23] Q. Yongzhi, A. C. Brown, D. R. Myers, S. Yumiko, R. G. Mannino, T. Reginald, A. Byungwook, E. T. Hardy, M. F. Kee, and K. Sanjay, Platelet mechanosensing of substrate stiffness during clot formation mediates adhesion, spreading, and activation, *Proc. Natl. Acad. Sci. USA* **111**, 14430 (2014).
- [24] Y. Chen, L. A. Ju, F. Zhou, J. Liao, L. Xue, Q. P. Su, D. Jin, Y. Yuan, H. Lu, S. P. Jackson, and C. Zhu, An integrin $\alpha_{IIb}\beta_3$ intermediate affinity state mediates biomechanical platelet aggregation, *Nat. Mater.* **18**, 760 (2019).
- [25] J. R. Byrnes and A. S. Wolberg, Red blood cells in thrombosis, *Blood* **130**, 1795 (2017).
- [26] S. Yesudasan and R. D. Averett, Recent advances in computational modeling of fibrin clot formation: A review, *Comput. Biol. Chem.* **83**, 107148 (2019).
- [27] A. L. Fogelson and R. D. Guy, Platelet-wall interactions in continuum models of platelet thrombosis: Formulation and numerical solution, *Math. Med. Biol.* **21**, 293 (2004).
- [28] M. Mehrabadi, D. N. Ku, and C. K. Aidun, A continuum model for platelet transport in flowing blood based on direct numerical simulations of cellular blood flow, *Ann. Biomed. Eng.* **43**, 1410 (2015).
- [29] N. A. Mody and M. R. King, Three-dimensional simulations of a platelet-shaped spheroid near a wall in shear flow, *Phys. Fluids* **17**, 113302 (2005).
- [30] W. Wang and M. R. King, Multiscale modeling of platelet adhesion and thrombus growth, *Ann. Biomed. Eng.* **40**, 2345 (2012).
- [31] Z. Wu, Z. Xu, O. Kim, and M. Alber, Three-dimensional multi-scale model of deformable platelets adhesion to vessel wall in blood flow, *Philos. Trans. R. Soc. B* **372**, 20130380 (2014).
- [32] I. V. Pivkin, P. D. Richardson, and G. E. Karniadakis, Blood flow velocity effects and role of activation delay time on growth and form of platelet thrombi, *Proc. Natl. Acad. Sci. USA* **103**, 17164 (2006).
- [33] K. Vahidkhah, S. Diamond, and P. Bagchi, Platelet dynamics in three-dimensional simulation of whole blood, *Biophys. J.* **106**, 2529 (2014).
- [34] T. Ye, N. Phan-Thien, C. T. Lim, L. N. Peng, and H. X. Shi, Hybrid smoothed dissipative particle dynamics and immersed boundary method for simulation of red blood cells in flows, *Phys. Rev. E* **95**, 063314 (2017).
- [35] G. S. Li, T. Ye, and X. J. Li, Parallel modeling of cell suspension flow in complex micro-networks with inflow/outflow boundary conditions, *J. Comput. Phys.* **401**, 109031 (2020).
- [36] T. Ye, L. N. Peng, and G. S. Li, Red blood cell distribution in a microvascular network with successive bifurcations, *Biomech. Model. Mechanobiol.* **18**, 1821 (2019).
- [37] T. Ye, H. X. Shi, N. Phan-Thien, C. T. Lim, and Y. Li, Numerical design of a microfluidic chip for probing mechanical properties of cells, *J. Biomech.* **84**, 103 (2019).
- [38] G. S. Li, T. Ye, S. T. Wang, X. J. Li, and R. U. Haq, Numerical design of a highly efficient microfluidic chip for blood plasma separation, *Phys. Fluids* **32**, 031903 (2020).

- [39] See Supplemental Material at <http://link.aps.org/supplemental/10.1103/PhysRevE.102.042410> for the details of the model validations and simulation videos, which includes Refs. [62–68].
- [40] R. M. Hochmuth and R. E. Waugh, Erythrocyte membrane elasticity and viscosity, *Ann. Rev. Physiol.* **49**, 209 (1987).
- [41] J. F. Zhang, P. C. Johnson, and A. S. Popel, Red blood cell aggregation and dissociation in shear flows simulated by lattice Boltzmann method, *J. Biomech.* **41**, 47 (2008).
- [42] R. D. Groot and P. B. Warren, Dissipative particle dynamics: Bridging the gap between atomistic and mesoscopic simulation, *J. Chem. Phys.* **107**, 4423 (1997).
- [43] T. Ye, H. X. Shi, N. Phan-Thien, and C. T. Lim, The key events of thrombus formation: Platelet adhesion and aggregation, *Biomech. Model. Mechanobiol.* **19**, 943 (2020).
- [44] M. B. Liu, J. R. Shao, and J. Z. Chang, On the treatment of solid boundary in smoothed particle hydrodynamics, *Sci. China Tech. Sci.* **55**, 244 (2012).
- [45] C. Misbah, Vacillating Breathing and Tumbling of Vesicles Under Shear Flow, *Phys. Rev. Lett.* **96**, 028104 (2006).
- [46] J. Dupire, M. Socol, and A. Viallat, Full dynamics of a red blood cell in shear flow, *Proc. Natl. Acad. Sci. USA* **109**, 20808 (2012).
- [47] Z. Zhang, J. Du, Z. Wei, Z. Wang, and M. Li, Effects of membrane deformability and bond formation/dissociation rates on adhesion dynamics of a spherical capsule in shear flow, *Biomech. Model. Mechanobiol.* **17**, 223 (2018).
- [48] J. Fritz, A. G. Katopodis, and K. D. Anselmetti, Force-mediated kinetics of single P-selectin/ligand complexes observed by atomic force microscopy, *Proc. Natl. Acad. Sci. USA* **95**, 12283 (1998).
- [49] A. Y. Maklygin, A. V. Priezhev, A. V. Karmenian, S. Y. Nikitin, I. S. Obolenskii, A. E. Lugovtsov, and K. Li, Measurement of interaction forces between red blood cells in aggregates by optical tweezers, *Quantum Electron.* **42**, 500 (2012).
- [50] H. Noguchi and G. Gompper, Vesicle dynamics in shear and capillary flows, *J. Phys.: Condens. Matter* **17**, S3439 (2005).
- [51] T. Ye, N. Phan-Thien, C. T. Lim, L. N. Peng, and H. X. Shi, Numerical studies of a red blood cell in rectangular microchannels, *J. Appl. Phys.* **122**, 084701 (2017).
- [52] C. S. Peskin, The immersed boundary method, *Acta Numer.* **11**, 479 (2002).
- [53] P. Español and M. Revenga, Smoothed dissipative particle dynamics, *Phys. Rev. E* **67**, 026705 (2003).
- [54] D. A. Fedosov, B. Caswell, and G. E. Karniadakis, A multiscale red blood cell model with accurate mechanics, rheology, and dynamics, *Biophys. J.* **98**, 2215 (2010).
- [55] L. Xiao, Y. Liu, S. Chen, and B. Fu, Effects of flowing rbcs on adhesion of a circulating tumor cell in microvessels, *Biomech. Model. Mechanobiol.* **16**, 597 (2017).
- [56] P. Bagchi, P. C. Johnson, and A. S. Popel, Computational fluid dynamic simulation of aggregation of deformable cells in a shear flow, *J. Biomech. Eng.* **127**, 1070 (2005).
- [57] B. Neu and H. J. Meiselman, Depletion-mediated red blood cell aggregation in polymer solutions, *Biophys. J.* **83**, 2482 (2002).
- [58] B. Chung, P. C. Johnson, and A. S. Popel, Application of chimera grid to modelling cell motion and aggregation in a narrow tube, *Int. J. Numer. Methods Fluids* **53**, 105 (2007).
- [59] Y. L. Liu and W. K. Liu, Rheology of red blood cell aggregation by computer simulation, *J. Comput. Phys.* **220**, 139 (2006).
- [60] T. Ye, N. Phan-Thien, B. C. Khoo, and C. T. Lim, A file of red blood cells in tube flow: A three-dimensional numerical study, *J. Appl. Phys.* **116**, 124703 (2014).
- [61] K. Rack, V. Huck, M. Hoore, D. A. Fedosov, S. W. Schneider, and G. Gompper, Margination and stretching of von Willebrand factor in the blood stream enable adhesion, *Sci. Rep.* **7**, 14278 (2017).
- [62] R. Skalak, P. R. Zarda, K. M. Jan, and S. Chien, Mechanics of rouleau formation, *Biophys. J.* **35**, 771 (1981).
- [63] J. Li, G. Lykotrafitis, M. Dao, and S. Suresh, Cytoskeletal dynamics of human erythrocyte, *Proc. Nat. Acad. Sci. USA* **104**, 4937 (2007).
- [64] P. Zihlerl and S. Svetina, Flat and sigmoidally curved contact zones in vesicle-vesicle adhesion, *Proc. Natl. Acad. Sci. USA* **104**, 761 (2007).
- [65] L. Xiao, S. Chen, C. Lin, and Y. Liu, Simulation of a single red blood cell flowing through a microvessel stenosis using dissipative particle dynamics, *Mol. Cell. Biomech.* **11**, 67 (2014).
- [66] R. Gu, X. Q. Wang, and M. Gunzburger, A two phase field model for tracking vesicle-vesicle adhesion, *J. Math. Biol.* **73**, 1293 (2016).
- [67] H. N. Polwaththe-Gallage, S. C. Saha, E. Sauret, R. Flower, and Y. Gu, A coupled SPH-DEM approach to model the interactions between multiple red blood cells in motion in capillaries, *Int. J. Mech. Mater. Des.* **12**, 477 (2016).
- [68] T. Ye and Y. Li, A comparative review of smoothed particle hydrodynamics, dissipative particle dynamics and smoothed dissipative particle dynamics, *Int. J. Comput. Meth.* **15**, 1850083 (2018).